Layer-by-Layer Assembly of Sintered $CdSe_xTe_{1-x}$ Nanocrystal Solar Cells

Brandon I. MacDonald,[†,‡] Alessandro Martucci,[¶] Sergey Rubanov,[§] Scott E. Watkins,[‡] Paul Mulvaney,[*,†] and Jacek J. Jasieniak[*,‡]

[†]School of Chemistry and Bio21 Institute, The University of Melbourne, Parkville, Victoria, 3010, Australia, [‡]Materials Science and Engineering, CSIRO, Bayview Avenue, Clayton, Victoria, 3168, Australia, [¶]Dipartimento di Ingegneria Meccanica Settore Materiali, Università di Padova, Via Marzolo, 9, 35131, Padova, Italy, and [§]Electron Microscopy Unit, Bio21 Institute, The University of Melbourne, Parkville, Victoria, 3010, Australia

ABSTRACT

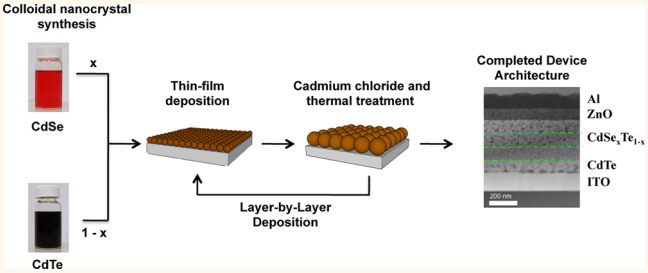

Alloying is a versatile tool for engineering the optical and electronic properties of materials. Here, we explore the use of CdTe and CdSe nanocrystals in developing sintered $CdSe_xTe_{1-x}$ alloys as bandgap tunable, light-absorbing layers for solution-processed solar cells. Using a layer-by-layer approach, we incorporate such alloyed materials into single- and graded-composition device architectures. Nanostructured solar cells employing $CdSe_xTe_{1-x}$ layers are found to exhibit a spectral response deeper into the IR region than bulk CdTe devices as a result of optical bowing and achieve power conversion efficiencies as high as 7.1%. The versatility of the layer-by-layer approach is highlighted through the fabrication of compositionally graded solar cells in which the [Se]:[Te] ratio is varied across the device. Each of the individual layers can be clearly resolved through cross-sectional imaging and show limited interdiffusion. Such devices demonstrate the importance of band-alignment in the development of highly efficient, nanostructured solar cells.

KEYWORDS: solar cell · nanocrystal · CdTe · $CdSe_xTe_{1-x}$ · layer-by-layer · solution-processed · sintered

Thin film metal chalcogenide solar cells represent a high-efficiency and cost-effective alternative to conventional silicon based photovoltaics. For instance, devices fabricated using cadmium telluride (CdTe) and copper indium gallium selenide (CIGS) based active layers have exhibited laboratory scale power conversion efficiencies up to 17.3%[1] and 20.3%,[2] respectively, at commercial production costs as low as US $0.75/Watt. Despite these successes, all such high-efficiency cells are manufactured using costly, vacuum-based deposition methods. One way to further lower the cost of thin film solar cells is to use solution-processing of colloidal semiconducting nanocrystals to deposit the individual layers in a device.

Of the various strategies for achieving this, the method which has yielded among the highest efficiency devices to date is the use of sintered nanocrystal layers. In this approach, the nanocrystals are deposited from solution as a thin film and are then chemically and/or thermally treated to induce large-scale grain growth.[3,4] This methodology combines the low-cost of solution processing with the excellent electronic properties of bulk inoganic semiconductors. Using a sintered nanocrystal absorber layer, power conversion efficiencies of 7% or higher have been achieved for cells based on CdTe, CIGS, and CZT(S,Se).[5−7]

The Shockley-Queisser limit for single and multijunction solar cells dictates that controlling the bandgap of individual absorbing layers is critical for achieving high efficiencies.[8,9] For solution-processed CIGS cells this has been achieved by varying the relative Ga content in the precursor materials.[6,10] In CZT(S,Se) based systems the bandgap has been tuned either by varying the sulfur to selenium ratio[11] or through the incorporation of germanium.[12] To date, there have been no examples of bandgap tuning in CdTe-based nanocrystal solar cells. Given that the CdTe bulk bandgap of 1.45 eV is nearly ideal for terrestrial applications, this is generally not a concern for devices with a single absorber layer. However, for its applications in tandem cells, bandgap control is an important consideration.

One approach to bandgap tuning in CdTe is through the incorporation of Se to create $CdSe_xTe_{1-x}$ alloys. In the past, such alloys have been fabricated by a number of methods, including electrodeposition, electron-beam evaporation, and colloidal nanocrystal synthesis.[13−15] While all of these reports

* Address correspondence to mulvaney@unimelb.edu.au, Jacek.Jasieniak@csiro.au.

Received for review February 29, 2012 and accepted June 12, 2012.

Published online June 12, 2012
10.1021/nn3009189

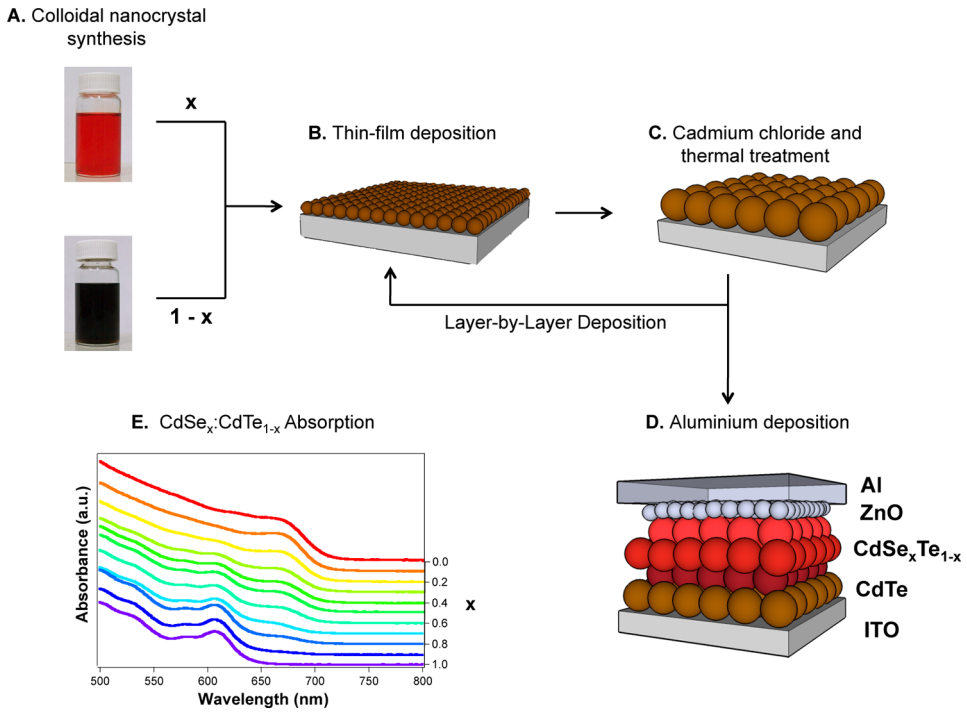

Figure 1. A schematic outline of the layer-by-layer process for making $CdSe_xTe_{1-x}$ nanocrystal solar cells. (A) CdSe and CdTe nanocrystals dispersed in pyridine/1-propanol are mixed at the desired ratio. (B) A thin film of $CdSe_x$:$CdTe_{1-x}$ is deposited by spin-coating onto the ITO substrate. (C) The thin film is subjected to a $CdCl_2$ treatment followed by thermal annealing to promote crystal growth. This process is repeated as necessary to yield the desired device composition and active layer thickness. (D) A schematic image of a completed device, which includes a layer of nanocrystalline ZnO and the evaporated aluminum top contact. (E) Absorption spectra of $CdSe_x$:$CdTe_{1-x}$ solutions.

have studied the effect of Se incorporation on the optical properties of $CdSe_xTe_{1-x}$, there have been few reports on the fabrication of solar cells using these alloy materials.[16,17] Of these, the most notable example used sublimed $CdSe_{0.7}Te_{0.3}$/$CdSe_{0.15}Te_{0.85}$ to create solar cells with a modest efficiency of 3.1%.[16]

The incorporation of alloyed layers into solar cells also allows for the fabrication of compositionally graded structures, with tunable bandgap and energy level alignment. Such compositional engineering is critical for obtaining high-efficiency CIGS devices, where a three-stage evaporation process is employed to vary the Ga/(In + Ga) ratio throughout the film.[18,19] This enhances both the open-circuit voltage (V_{oc}) and short-circuit current density (J_{sc}) of the device through reduced charge recombination and increased light absorption, respectively.[20] More recently, the graded device concept has been extended to solution-processed organic solar cells, through a series of complementary donor materials[21] and to PbS quantum dot devices, where bandgap grading was accomplished through variation of the QD diameter.[22]

Here we demonstrate the first use of compositional grading in sintered nanocrystal solar cells, using $CdSe_xTe_{1-x}$ alloys formed by sintering thin films containing mixtures of CdTe and CdSe nanocrystals. While it is possible to directly synthesize $CdSe_xTe_{1-x}$ nanocrystals with tunable composition,[15] it is generally accepted that it is significantly harder to reproducibly control the exact stoichiometry in such alloyed systems.[23] For this reason, the use of binary components provides a more facile approach for developing various alloys. We demonstrate this factor by providing a detailed structural, optical, and electronic-level characterization of $CdSe_xTe_{1-x}$ thin films. Through the use layer-by-layer processing, such alloys are incorporated within both single- and graded-composition solar cell architectures, achieving power conversion efficiencies as high 7.1%.

RESULTS AND DISCUSSION

$CdSe_xTe_{1-x}$ Thin Film Fabrication and Characterization. The process used for the fabrication of $CdSe_xTe_{1-x}$ thin films and solar cells is outlined in Figure 1. First, stock solutions of colloidal CdTe and CdSe nanocrystals passivated with pyridine were mixed appropriately to yield $CdSe_x$:$CdTe_{1-x}$ dispersions. As expected, the size-confined absorption spectra of these solutions showed a decreasing intensity in the first excitonic peak of CdSe, at 605 nm, and a concordant increase of the CdTe peak, at 662 nm, as x was varied from 1 (pure CdSe) to 0 (pure CdTe) (Figure 1E). Following deposition *via* spin-coating, the thin films were treated with $CdCl_2$ and annealed in air at 350 °C to promote large-scale grain growth and alloying (*vide infra*).[5] This process was repeated in a layer-by-layer fashion up to four times, until the desired thickness and active layer composition

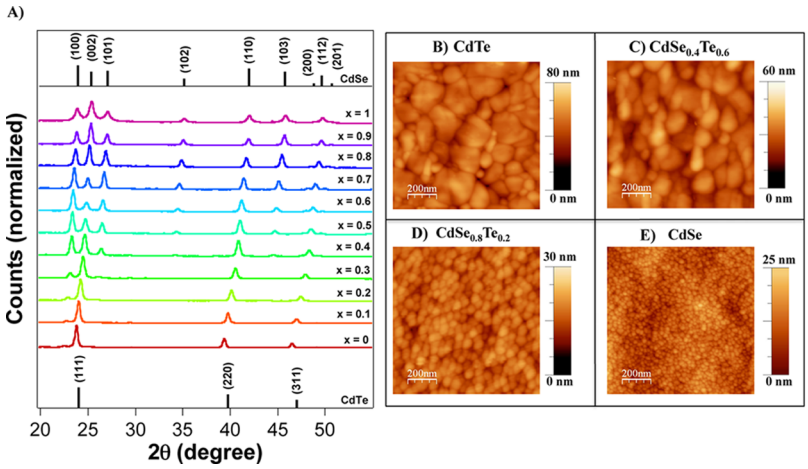

Figure 2. (A) X-ray diffraction patterns for ~100 nm thick $CdSe_xTe_{1-x}$ thin films which have been treated with $CdCl_2$ and annealed at 350 °C for 30 s as well as standard values for cubic CdTe (JCPDS #75-2086) and hexagonal CdSe (JCPDS #08-0459). (B–E) Tapping mode AFM images of CdTe, $CdSe_{0.4}Te_{0.6}$, $CdSe_{0.8}Te_{0.2}$, and CdSe films, respectively. For all samples, two layers were deposited, with $CdCl_2$ treatment and thermal annealing step performed after each layer. The total film thickness was ~200 nm.

was achieved. Devices were completed by spin-coating of a 60 nm thick layer of colloidal ZnO nanocrystals followed by thermal evaporation of an aluminum back contact.

Before embarking on the characterization of such alloyed devices, we first turn our attention to understanding the structural and electronic level properties of the alloyed layers. The crystal structure of sintered $CdSe_xTe_{1-x}$ films was studied by grazing angle X-ray diffraction (XRD). Neat CdTe and CdSe films were found to exist in their thermodynamically most stable cubic and hexagonal crystal phases, respectively (Figure 2A).[24] From the XRD patterns of the Te rich samples it is clear that all of the scattering contributions associated with the CdTe shift toward higher 2θ values with increasing x. This is consistent with the formation of an alloyed cubic phase that possesses an increasingly smaller lattice constant. For x = 0.3 and above we do, however, observe the emergence of a secondary phase that is characteristic of a hexagonal crystal structure (Supporting Information, Figure S1). The overlap of the (111) peak of the cubic phase with the (100) peak of the hexagonal phase for the most Se rich samples, prevents us from unequivocally identifying the upper boundary of this dual phase region. These observations are in agreement with previous reports on bulk $CdSe_xTe_{1-x}$ alloys.[25,26]

The formation of $CdSe_xTe_{1-x}$ alloys is accompanied by large-scale grain growth through nanocrystal sintering. This sintering process tends to create large structural defects in nanocrystal thin films which can lead to the short-circuiting of completed devices. This problem can be overcome through the use of layer-by-layer processing, which enables defects to be filled-in or overcoated by subsequent depositions. Atomic force microscopy (AFM) images of layer-by-layer deposited $CdSe_xTe_{1-x}$ show that nanocrystalline layers with rms roughness of between 8.6 nm (CdTe) and 4.2 nm (CdSe) are obtained (Figure 2(B–E)). Having started with 4-5 nm nanoparticles, there is clear evidence of grain growth following $CdCl_2$ treatment and annealing at 350 °C; however, the extent of grain growth does decrease with increasing Se content, with the average crystal size decreasing from 38 nm for CdTe to 17 nm for CdSe, as determined from XRD using the Scherrer equation. This is consistent with AFM images which exhibit the same trend toward smaller grains with increasing Se content (Supporting Information, Table T1). We attribute this partially to the larger lattice energy of CdSe (749 kcal/mol) compared to CdTe (680 kcal/mol).[27] Since the surface energies for both CdSe and CdTe are similar,[28] this would cause the CdSe to exhibit a higher activation energy for recrystallization and grain growth relative to CdTe,[29] thus reducing its size under identical annealing conditions. We also note that both CdSe and CdTe are known to oxidize upon annealing in air, forming surface oxides such as $CdSeO_3$[30] and $CdTeO_3$[31] respectively. It is expected that the formation of these oxide species will restrict further grain growth from occurring.[32] Therefore, the intrinsic differences between the rates of recrystallization and oxidation across the investigated composition range are believed to cause the observed variation of crystallite sizes.

To investigate the effects of alloy formation on the optical properties of $CdSe_xTe_{1-x}$ thin films, we performed UV–visible absorption measurements. For all compositions, plots of $(\alpha h\nu)^2$ *versus* photon energy have a linear onset, indicating a direct bandgap (Figure 3A). The optical bandgap was determined by extrapolating the linear region of this plot to the x-axis. For the region in which both cubic and hexagonal crystal phases are observed we see only a single absorption feature which is most likely an average of the two phases.

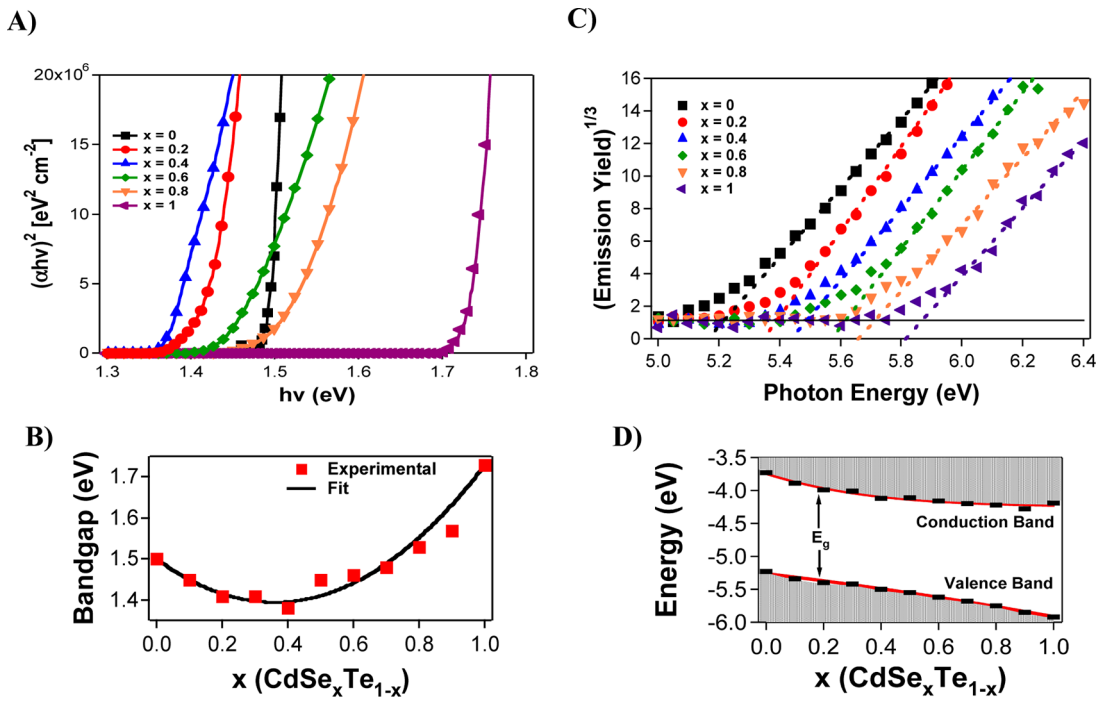

Figure 3. (A) Selected plots of $(\alpha h\nu)^2$ *vs* $h\nu$ as a function of $CdSe_xTe_{1-x}$ composition. Measurements were made on 200 nm thick films which had been $CdCl_2$ treated and annealed at 350 °C for 30 s. (B) Bandgap of $CdSe_xTe_{1-x}$ alloy films as a function of composition (red squares) as well as a fit to the standard bowing equation. Experimental values were determined by extrapolating the linear portion of $(\alpha h\nu)^2$ *vs* $h\nu$ plots to zero. (C) PESA spectra of films with varying $CdSe_xTe_{1-x}$ composition. (D) Valence band maxima and conduction band minima as a function of alloy composition. Valence band levels were determined directly from PESA, while conduction band levels were approximated by combining the valence band levels with the experimentally determined optical bandgaps. Solid red lines are a guide to the eye.

Plotting the bandgap as a function of composition reveals clear optical bowing (Figure 3B), that is, a parabolic variation of the bandgap with alloy composition. This effect is due to the disorder created by the presence of mulitple anions (or cations) in the crystal lattice[33] and has been observed both theoretically[34,35] and experimentally[25,26] in $CdSe_xTe_{1-x}$ and other semiconducting alloys.[36,37] By tuning the $CdSe_xTe_{1-x}$ film composition we are able to vary the optical bandgap from 1.38 eV (absorption onset ~899 nm) to 1.73 eV (absorption onset ~717 nm).

The relationship between optical bandgap and alloy composition can be expressed using the standard bowing equation $E_g(x) = bx(1 - x) + (E_{CdTe} - E_{CdSe})x - E_{CdTe}$, where b is the optical bowing parameter and E_{CdSe} and E_{CdTe} are the bulk bandgaps of CdSe and CdTe, respectively. Fitting our results to this equation yields a bowing parameter of 0.81 eV, in good agreement with literature values which vary from 0.59 to 0.91 eV.[14,38]

The spectral tunability of the $CdSe_xTe_{1-x}$ layers is an appealing property for their use within solar cells. To effectively utilize these layers in these such devices, it is vital that the electronic structure is first understood. To accomplish this we have studied $CdSe_xTe_{1-x}$ films using photoelectron spectroscopy in air (PESA). In PESA, the yield of photoemitted electrons is measured as a function of incident photon energy. From the cubic root of this photoemission yield, the ionization energy of inorganic semiconductor samples can be determined.[39] Typical PESA plots for $CdSe_xTe_{1-x}$ films are shown in Figure 3C. From these results we see that the ionization energy steadily shifts to higher energies with increasing Se content, from 5.23 eV for CdTe to 5.92 eV for CdSe.

The corresponding conduction band edges of the samples can be approximated by adding the optical bandgap to the ionization energy. In contrast to the nearly linear variation observed in ionization energy with changing composition, the conduction band edge initially shifts to higher energies with increasing x before leveling off at $x \geq 0.4$ (Figure 3D). These results are consistent with theoretical studies of $CdSe_xTe_{1-x}$, which have shown that the majority of filled states near the valence band edge are located on the anionic atoms, in particular Te, while states near the conduction band edge are predominantly located on the Cd atoms.[38] In our films, where only the Se to Te ratio is changing, it is therefore expected that varying composition will have a much greater effect on the valence band structure.

Solar Cell Performance. Having studied the optical and electronic properties of sintered, nanocrystalline $CdSe_xTe_{1-x}$ alloys we then examined their performance in solution-processed solar cells fabricated using the layer-by-layer assembly method outlined in Figure 1. Our aim in this work was not to optimize for

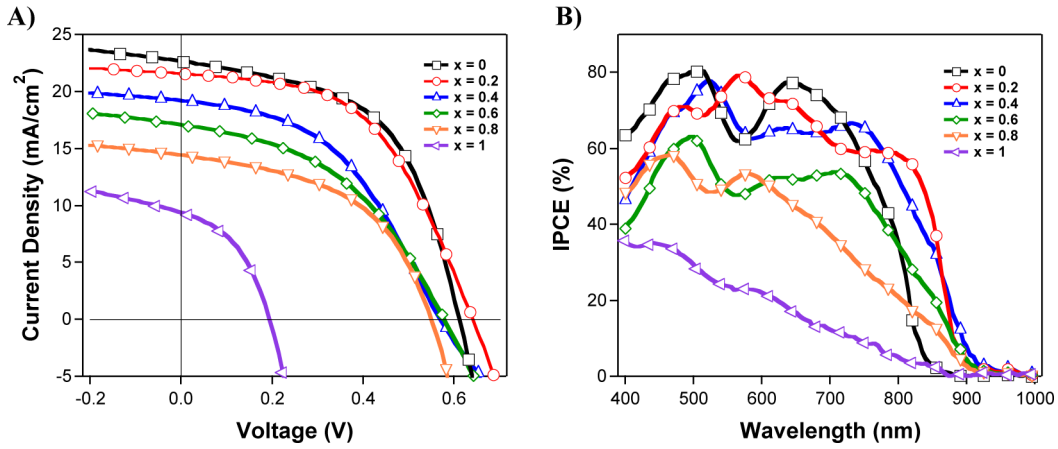

Figure 4. (A) Current−voltage curves for selected $CdSe_xTe_{1-x}$ solar cells. The structure of the device stack was ITO/CdTe(∼100 nm)/$CdSe_xTe_{1-x}$(∼300 nm)/ZnO(60 nm)/Al(100 nm). All CdTe and $CdSe_xTe_{1-x}$ layers were treated with $CdCl_2$ and annealed at 350 °C for 30 s in air. The ZnO layer was annealed in air at 300 °C for 2 min. (B) IPCE curves for the same devices. The oscillations oberved in the photoresponse spectra of these solar cells is a direct result of thin film interference effects.

TABLE 1. Performance Characteristics of Solar Cells with Varying Alloy Composition[a]

device structure	J_{sc} (mA/cm^2)	V_{oc} (V)	FF	efficiency
CdTe(400 nm)/ZnO	22.6	0.61	0.53	7.3%
CdTe(100 nm)/$CdSe_{0.1}Te_{0.9}$(300 nm)/ZnO	20.3	0.61	0.57	7.1%
CdTe(100 nm)/$CdSe_{0.2}Te_{0.8}$(300 nm)/ZnO	21.6	0.64	0.51	7.0%
CdTe(100 nm)/$CdSe_{0.3}Te_{0.7}$(300 nm)/ZnO	19.5	0.63	0.47	5.8%
CdTe(100 nm)/$CdSe_{0.4}Te_{0.6}$(300 nm)/ZnO	18.7	0.57	0.46	4.9%
CdTe(100 nm)/$CdSe_{0.5}Te_{0.5}$(30 0 nm)/ZnO	16.0	0.56	0.49	4.4%
CdTe(100 nm)/$CdSe_{0.6}Te_{0.4}$(300 nm)/ZnO	16.7	0.58	0.44	4.2%
CdTe(100 nm)/$CdSe_{0.7}Te_{0.3}$(300 nm)/ZnO	15.2	0.59	0.54	4.8%
CdTe(100 nm)/$CdSe_{0.8}Te_{0.2}$(300 nm)/ZnO	14.0	0.55	0.49	3.8%
CdTe(100 nm)/$CdSe_{0.9}Te_{0.1}$(300 nm)/ZnO	11.9	0.49	0.42	2.5%
CdTe(100 nm)/CdSe(300 nm)/ZnO	9.4	0.19	0.41	0.7%

[a] All cells consist of an ITO front electrode and 100 nm thick Al back electrode. Current−voltage measurements were taken under 100 mW/cm^2 AM1.5 conditions and have been corrected for spectral mismatch.

high device efficiencies but rather to investigate the influence of using alloyed layers within a fixed set of device fabrication parameters. Following each deposition, the devices were treated with a $CdCl_2$ solution to remove the pyridine ligands from the nanocrystal surface and to promote crystal growth upon annealing. Each layer was annealed in air at 350 °C, the temperature we have previously found to result in optimal performance for CdTe devices,[5] for 30 s. A completed device consists of a single CdTe layer, three $CdSe_xTe_{1-x}$ layers, and a nanocrystalline ZnO layer. Using a CdTe buffer layer between the semiconducting layers and the underlying substrate ensures that there is an identical rectifying interface with ITO for all of the alloy containing devices. This enables interfacial effects between the semiconducting layers and ITO to be minimized, which in turn permits the role of the alloy layers on solar cell performance to be isolated. Meanwhile, the highly n-type ZnO layer acts as an effective hole blocking layer and enhances charge separation within the active layer by creating an extended depletion region within the device.

Current−voltage curves for $CdSe_xTe_{1-x}$ containing devices are shown in Figure 4A, with performance characteristics summarized in Table 1. The highest performance is obtained for CdTe-only devices, with a power conversion efficiency (PCE) of 7.3%. Increasing Se content results in the device performance decreasing, primarily due to lower J_{sc} values. A comparison of the absorption characteristics of these devices indicates that this arises due to lower light absorption in films with higher Se content (Supporting Information, Figure S2). By contrast, the open-circuit voltage is essentially independent of the alloy layer composition. This result is consistent with the absorbing layers of the device being fully depleted under short-circuit conditions, as previously observed in a pure CdTe/ZnO nanocrystal system.[5] In such a case the built-in voltage of the device is governed by the work function difference between the ITO and the heavily doped ZnO layer, which is of the order of 0.5−0.6 V. This is in good agreement with the open-circuit voltage values obtained for our alloy containing devices. Overall, these results suggest that by optimizing the thickness and therefore the spectral absorption of the alloy layers, high efficiency devices may be obtained.

For devices containing CdSe rather than alloy layers, the open-circuit voltage is significantly lower at only 0.19 V. In such devices it appears that the built-in field is generated across the CdTe layer alone and does not extend into the CdSe. As a consequence, the V_{oc} is limited by the thickness of the CdTe layer. Indeed for devices without a CdTe buffer between the ITO and CdSe no photovoltage is obtained, while for devices with thicker CdTe layers (but fixed overall thickness) the open-circuit voltage and overall performance are improved (Supporting Information, Figure S3). At this point we are uncertain as to why the behavior of these

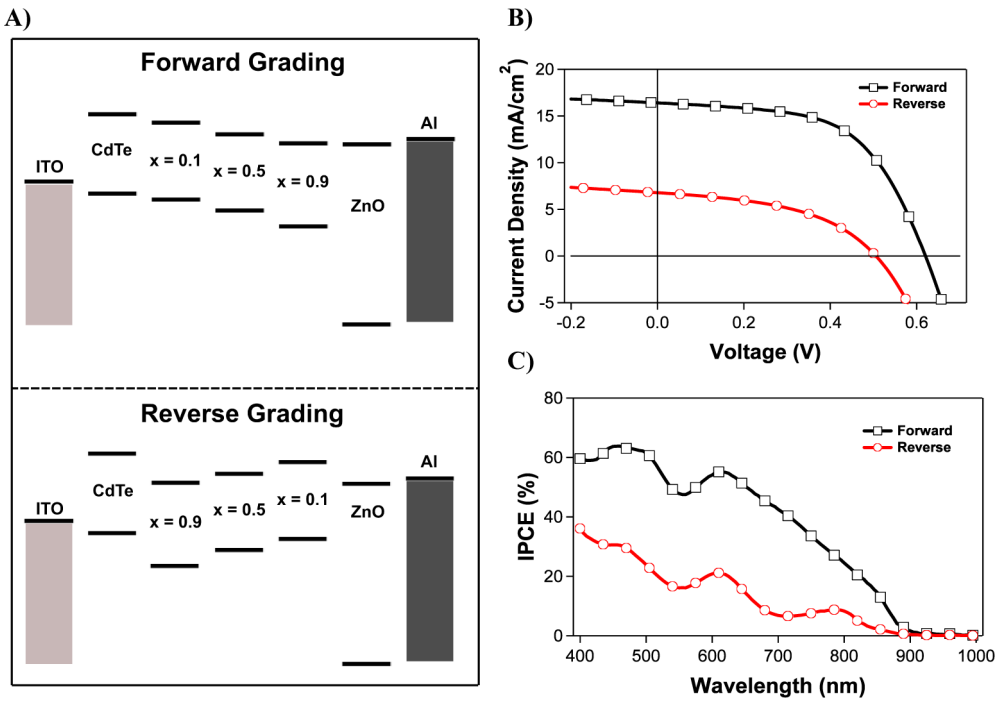

Figure 5. (A) Flat-band energy diagrams for forward and reverse graded nanocrystal solar cells. (B) Current−voltage curves of graded cells under 1 sun illumination. In both devices the thickness of each individual $CdSe_xTe_{1-x}$ layer was ~100 nm for a total absorber layer thickness of ~400 nm. The thickness of the ZnO layer was 60 nm. (C) IPCE spectra for the same graded devices. The forward graded structure exhibits superior performance across the entire spectral range.

devices differs from that of the alloy containing devices, although it may be related to the relative reduction of crystal sizes observed in CdSe films at 350 °C.

Incident photon-to-current efficiency (IPCE) measurements of the above devices clearly exhibit the effect of optical bowing on the spectral response of $CdSe_xTe_{1-x}$ containing solar cells. In CdTe-only devices the IPCE approaches zero near the bulk CdTe absorption edge of ~860 nm, while for alloyed devices values as high as 30% are obtained at this wavelength, with responses extending to as far as ~900 nm (Figure 4B). This result clearly demonstrates that the $CdSe_xTe_{1-x}$ layers are contributing to the photocurrent of the device. Interestingly, devices with higher Se content ($x = 0.6, 0.8$) also exhibit an extended spectral response despite the fact that the bandgaps of these alloys are similar to that of CdTe (Supporting Information, Figure S4). We believe that this is due to local variations in composition, both at the CdTe/$CdSe_xTe_{1-x}$ interface and within the alloy layers, which will affect the absorption properties and photoresponse of the device.

Compositionally Graded Solar Cells. Using the layer-by-layer method for developing solution processed solar cells it is possible to create structures with vertical composition gradients, a task which can not be readily achieved using a single layer deposition method. In this work, such grading was achieved by simply varying the composition of the nanocrystal dispersion used in each deposition step. Using this method we created cells in a "forward" graded architecture, with favorable band alignment and a "reverse" graded architecture, where band alignment is unfavorable (Figure 5A). The current−voltage characteristics of these graded nanocrystal devices are presented in Figure 5B and summarized in Table 2. In the forward-graded cell a power conversion efficiency of 5.4% is obtained. Examination of the performance parameters reveals that the open-circuit voltage and fill factor of this cell are comparable to those of our highest efficiency devices and that device performance is primarily limited by a relatively low J_{sc} of 15.5 mA/cm^2. As explained above, this is directly due to the reduced absorption of the $CdSe_xTe_{1-x}$ layers compared to pure CdTe films.

In comparison, the reverse-graded cell exhibits inferior performance across all device parameters. The resulting PCE of 1.5% is substantially lower than both the forward-graded cell and any of the non-graded, alloy containing devices. This observation is consistent with poor charge transport through the cell due to the unfavorable band structure. On the basis of

TABLE 2. Performance Characteristics of Forward and Reverse Graded Nanocrystal Solar Cells[a]

device structure	J_{sc} (mA/cm^2)	V_{oc} (V)	FF	efficiency
forward	15.5	0.62	0.56	5.4%
reverse	6.5	0.50	0.46	1.5%

[a] All measurements were taken under 100 mW/cm^2 AM1.5 illumination and have been corrected for spectral mismatch.

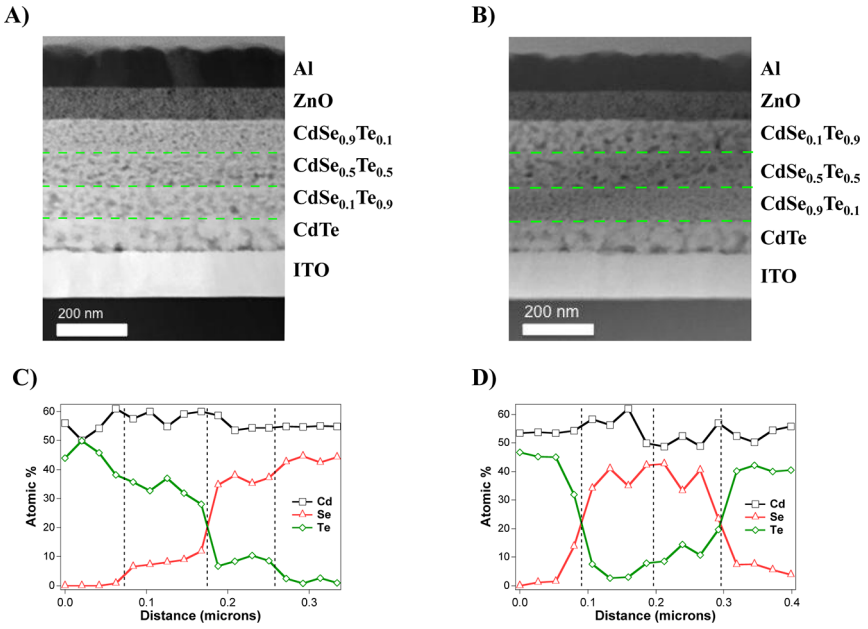

Figure 6. (A,B) Cross-sectional dark-field STEM images of forward and reverse graded devices, respectively. The dashed green lines serve as a guide to the eye. (C) Cross-sectional EDS profile of the CdTe/$CdSe_xTe_{1-x}$ layers in a forward graded device. (D) Cross-sectional EDS profile of the CdTe/$CdSe_xTe_{1-x}$ layers in a reverse graded device. Dashed lines indicate the boundaries between device layers.

the energy levels presented in (Figure 5A) this cell would not be expected to deliver any meaningful photovoltaic performance. However, this simple diagram ignores effects such as band-bending, Fermi level pinning, and the presence of trap states, which will make the true band structure of a device much more complex. Evidently this does allow for partial extraction of photogenerated carriers from within the device. To further examine the performance difference between the graded structures, we have examined their IPCE spectra (Figure 5C). Both devices show an extended response relative to CdTe and follow roughly the same spectral profile, with the forward-graded device clearly exhibiting superior response across the entire spectral range. As the absorption profiles of the devices are nearly identical (Supporting Information, Figure S5), we can exclude light absorption differences as the cause of this effect. Instead it is clear that by changing the vertical composition and electronic structure of the device, the efficiency by which photogenerated charge carriers are collected can be strongly influenced. While the overall efficiency of these devices is relatively low, these results demonstrate the utility of layer-by-layer assembly in the fabrication of compositionally engineered solar cells.

To better appreciate the structural and compositional characteristics of our graded solar cells, we employed dark-field scanning transmission electron microscopy (STEM) on device cross sections prepared using a focused ion beam (FIB). In the forward-graded structure, each of the four distinct $CdSe_xTe_{1-x}$ layers can be clearly be distinguished (Figure 6A, Supporting Information, Figure S6). The image also shows that with each successive layer, and corresponding increase in Se content, the average grain size decreases; an observation that is consistent with AFM topographies. In this structure, each consecutive layer is thermally annealed for a lesser total time. This raises the question whether the final grain size obtained is simply a function of total annealing time. By examining a reverse-graded structure we can see that this is not the case (Figure 6B). Once again, each of the $CdSe_xTe_{1-x}$ layers can clearly be resolved and it is seen that layers with higher Se content exhibit less grain growth. This is consistent with results that we have obtained for CdTe films, which show an initially rapid increase in grain size upon annealing, but only very limited further growth with extended heating. It is likely that the grain growth in these films is limited by the formation of surface oxides such as $CdTeO_3$, the presence of which can be seen from XRD (Supporting Information, Figure S7). This surface oxidation is known to occur upon annealing of CdTe in air,[31] and given the high surface area to volume of nanocrystalline films it is to be expected that this process will occur rapidly.

The composition of the graded cells was measured using energy dispersive X-ray spectroscopy (EDS). In both devices we observe a cadmium-rich composition, approximately 55 atom %, throughout the device (Figure 6C,D). At this point we are uncertain if this excess Cd is found in the crystal bulk or if a Cd-rich surface layer is created by the $CdCl_2$ treatment. Examining the chalcogenide content of the forward-graded device we see that both the Se and Te concentrations vary throughout the device in a nearly stepwise manner. In both the CdTe and $CdSe_{0.1}Te_{0.9}$ layers the

measured composition is close to the expected value. For the upper two alloy layers we see that the composition is Se-rich compared to the predicted values. This is especially true for the layer with a nominal composition of $CdSe_{0.5}Te_{0.5}$, where instead of equal Se and Te concentrations we measure a [Se]/[Te] ratio of approximately 4:1. In the reverse-graded cell we observe a similar trend, where the $CdSe_{0.5}Te_{0.5}$ layer is found to have much higher Se than Te content. It appears that in a graded solar cell, a 1:1 ratio of [Se]:[Te] is not a stable composition and that a more favorable Se-rich composition is obtained. This may arise through atomic diffusion with other device layers or through the loss of volatile Te species during the annealing process. Interestingly, this composition is within the range where multiple phases are observed in XRD. This structural variation may also hold answers to the chemical composition. Despite this uncertainty, we see that in this system compositional grading has been successfully demonstrated with limited interlayer diffusion. We believe that this relative lack of diffusion can again be attributed to the formation of surface oxides, as it has been shown previously that $CdTeO_3$ formation prevents chalcogenide interdiffusion in CdS/CdTe solar cells without inhibiting device performance.[40] Overall these results demonstrate the utility of layer-by-layer assembly in fabricating complex, multilayered device architectures.

CONCLUSIONS

We have fabricated thin films of $CdSe_xTe_{1-x}$ from mixtures of CdSe and CdTe nanocrystals. These films exhibit optical bowing, which allows their bandgap to be tuned as a function of alloy composition. Using layer-by-layer assembly these $CdSe_xTe_{1-x}$ films have been incorporated into sintered photovoltaic devices that exhibit an extended NIR spectral response relative to CdTe-only cells with efficiencies as high as 7.1%. Furthermore, we have demonstrated that this method can be effectively used to develop graded multilayered structures, in which compositional control is used to govern charge flow within photovoltaic devices. Ultimately, the concepts presented in this work will be useful in developing next generation nanocrystalline solar cells that require alloyed and/or graded compositional control.

METHODS

Chemicals. Cadmium oxide (CdO, Aldrich, 99.99%), tellurium powder (Aldrich, 99.9%), selenium powder (Aldrich, 99.99%), oleic acid (Aldrich, 90%), oleylamine (Pfaltz and Bauer, 97%) trioctylphosphine (TOP, Aldrich, 90%), 1-octadecene (ODE, Aldrich, 90%), bis-(2,2,4-trimethylpentyl) phosphinic acid (TMPPA, Cytec Specialty Chemicals), tetramethylammonium hydroxide (Aldrich, 20% in methanol), and zinc acetetate dihydrate (BDH Laboratory Supplies, 99.5%) were used in the preparations described here. All solvents were of analytical grade and purchased from Univar. All chemicals and solvents were used without further purification.

Nanocrystal Synthesis. CdTe nanocrystals were synthesized following a protocol reported elsewhere.[41] Briefly, 0.48 g of CdO, 4.24 g of oleic acid and 60 g of ODE were heated under vacuum to 80 °C at which point the flask was purged with nitrogen. The solution was heated to 260 °C and maintained at this temperature until it turned clear. At this point a solution of 240 mg of Te dissolved in 5 mL of trioctylphosphine was rapidly injected. The solution was then cooled to room temperature naturally, resulting in CdTe nanocrystals of ~4.3 nm. CdSe nanocrystals were synthesized following the method of Van Embden *et al.*[42] In a typical synthesis 0.30 g of CdO, 4.0 g of oleic acid and 60 g of ODE were heated under vacuum to 80 °C at which point the flask was purged with nitrogen. The solution was heated to 305 °C, at which point a solution of 0.45 g Se dissolved in 4.8 g TOP, 2.0 g oleylamine, 3 g TMPPA, and 3 g ODE was rapidly injected. The solution was then cooled naturally, resulting in CdSe nanocrystals of ~4.6 nm diameter. ZnO nanocrystals were synthesized following the method of Wood *et al.*[43] In a typical synthesis 0.44 g of zinc acetate dihydrate was added to 40 mL of ethanol and heated at 60 °C for approximately 30 min. Following this, 2 mL of tetramethylammonium hydroxide (20% in methanol) in 10 mL of ethanol was added to the solution dropwise over 5 min. The ZnO nanocrystal solution was heated at 60 °C for a further 30 min, resulting in ZnO nanocrystals with ~5 nm diameter.

Washing and Ligand Exchange. Both CdTe and CdSe NCs were washed by precipitating with ethanol and redispersing in toluene. For ligand exchange, the nanocrystals were precipitated with ethanol and redispersed in pyridine at a concentration of approximately 10 mg/mL. This solution was placed under nitrogen and heated under reflux overnight. Upon cooling, the pyridine capped CdTe or CdSe NCs were precipitated with cyclohexane and redispersed in a 1:1 (v/v) solution of pyridine/1-propanol. The mass concentration of these solutions was determined by slowly evaporating a known volume to dryness. From these values CdSe/CdTe solutions of an appropriate ratio were made. ZnO NCs were washed by precipitating with cyclohexane and redispersing in 1-propanol at an appropriate concentration. All nanocrystal dispersions were filtered with a Whatman Puradisc 25 GD filter prior to deposition.

Device Fabrication. ITO-coated glass (Lumtec, 5 Ω/cm^2) was cleaned by successively sonicating for 20 min each in distilled water, acetone and then isopropyl alcohol. The substrates were then UV-ozone treated for 10 min immediately prior to deposition. Nanocrystal solutions were spin-cast onto the ITO-coated glass slides at 800 rpm for 30 s. The substrates were then placed on a hot plate at 150 °C for 2 min, then immediately dipped into a 60 °C solution of saturated $CdCl_2$ in methanol for 10 s, rinsed with 1-PrOH, and finally dried under a nitrogen stream. The resulting nanocrystal thin films were sintered by placing the substrates onto a hot plate at 350 °C for 30 s. This process was repeated a total of four times to yield a film thickness of 300–400 nm. A ZnO layer of 60 nm was then spin-cast at 800 rpm for 30 s and heated at 300 °C for 2 min. All film deposition and treatment steps were performed in air. Aluminum contacts, 100 nm thick, were deposited *via* thermal evaporation through a shadow mask at pressures below 2×10^{-6} mbar. The total device area, as defined by the overlap between the ITO and Al electrodes, was determined to be 0.105 cm^2. Connection to the ITO electrode was made by manually scratching off a small amount of the active layer. The completed devices were encapsulated with glass and a UV-cured epoxy (Summers Optical, Lens Bond type J-91) by exposing the devices to 365 nm UV-light inside a glovebox for 10 min. Following encapsulation the devices were transferred to air for testing.

Characterization. Absorbance spectra were collected with a Varian Cary 5E spectrophotometer. The zero baseline measurements for all thin film measurements was air. AFM images were

taken using a Nanoscope III system (Veeco) and analyzed using WSxM v5.0 software.[44] X-ray diffraction data was obtained using a Philips diffractometer equipped with glancing-incidence X-ray optics. The analysis was performed at 0.5° incidence, using CuKα Ni filtered radiation at 30 kV and 40 mA. Crystal sizing from XRD was performed using multipeak Scherrer analysis with a shape factor of 0.9. For CdTe sizing the (111), (220), and (311) peaks were used, while for CdSe the (100), (110), and (103) peaks were used. Peak fitting was peformed using a Lorentzian function. PESA measurements were taken using a Riken Keiki AC-2 Photoelectron spectrometer. Annealing was performed on a calibrated titanium hot plate from Harry Gestigkeit GmbH with a temperature accuracy of ±10 °C. Cross-sectional STEM samples were prepared using a focused ion beam (FIB) lift-off technique, described elsewhere.[45] The samples were examined using an FEI Tecnai TF20 transmission electron microscope operated at 200 keV. Elemental analysis was performed in STEM mode using an EDAX X-ray detector with ultrathin window.

Solar cells were tested using an Oriel solar simulator with a 1000 W Xe lamp filtered to give an output of 100 mW/cm^2 at AM1.5. The lamp was calibrated using a Si reference cell from Peccell Ltd. which was subsequently cross-calibrated with a KG5 filtered reference cell traceable to the National Renewable Energy Laboratory. Electrical connections to the cells were made using alligator clips. The devices were tested using a Keithley 2400 sourcemeter controlled by Labview software. All current−voltage measurements have been corrected for spectral mismatch. IPCE measurements were performed using a customized Newport IPCE setup with no light biasing. Measurements were made under short-circuit conditions and referenced to a calibrated Si photodiode (Peccell Limited, S1337−1010BQ).

Conflict of Interest: The authors declare no competing financial interest.

Acknowledgment. The authors would like to thank Dr. A. Morfa for fruitful discussions. B.M. wishes to acknowledge the University of Melbourne for MIFRS and MRS scholarships and CSIRO for a Ph.D. studentship. This work was funded through the Flexible Electronics Theme of the CSIRO Future Manufacturing Flagship as part of an Office of the Chief Executive Postdoctoral Fellowship to J.J. J.J. would also like to acknowledge support through DP110105341. P.M. acknowledges support through DP0985325 and FF0561486.

Supporting Information Available: Absorption spectra of single and compositionally graded solar cells, current−voltage curves of CdTe/CdSe/ZnO devices with varying CdTe and CdSe thicknesses, bandgap determination from IPCE measurements, bright-field TEM images of graded devices and additional XRD measurements. This material is available free of charge *via* the Internet at http://pubs.acs.org.

REFERENCES AND NOTES

1. "First Solar Sets World Record for CdTe Solar PV Efficiency", First Solar Press Release, July 26, 2011; http://investor.firstsolar.com (accessed 10.01.12).
2. Jackson, P.; Hariskos, D.; Lotter, E.; Paetel, S.; Wuerz, R.; Menner, R.; Wischmann, W.; Powalla, M. New World Record Efficiency for Cu(In,Ga)Se_2 Thin-film Solar Cells Beyond 20%. *Prog. Photovoltaics Res. Appl.* **2011**, *19*, 894–897.
3. Gur, I.; Fromer, N. A.; Geier, M. L.; Alivisatos, A. P. Air-Stable All-Inorganic Nanocrystal Solar Cells Processed from Solution. *Science* **2005**, *310*, 462–465.
4. Olson, J. D.; Rodriguez, Y. W.; Yang, L. D.; Alers, G. B.; Carter, S. A. CdTe Schottky Diodes from Colloidal Nanocrystals. *Appl. Phys. Lett.* **2010**, *96*, 3.
5. Jasieniak, J.; MacDonald, B. I.; Watkins, S. E.; Mulvaney, P. Solution-Processed Sintered Nanocrystal Solar Cells *via* Layer-by-Layer Assembly. *Nano Lett.* **2011**, *11*, 2856–2864.
6. Guo, Q.; Ford, G. M.; Hillhouse, H. W.; Agrawal, R. Sulfide Nanocrystal Inks for Dense Cu($In_{1-x}Ga_x$)($S_{1-y}Se_y$)$_2$ Absorber Films and Their Photovoltaic Performance. *Nano Lett.* **2009**, *9*, 3060–3065.
7. Guo, Q.; Ford, G. M.; Yang, W. C.; Walker, B. C.; Stach, E. A.; Hillhouse, H. W.; Agrawal, R. Fabrication of 7.2% Efficient CZTSSe Solar Cells Using CZTS Nanocrystals. *J. Am. Chem. Soc.* **2010**, *132*, 17384–17386.
8. Shockley, W.; Queisser, H. J. Detailed Balance Limit of Efficiency of p−n Junction Solar Cells. *J. Appl. Phys.* **1961**, *32*, 510–519.
9. Vos, A. D. Detailed Balance Limit of the Efficiency of Tandem Solar Cells. *J. Phys. D: Appl. Phys.* **1980**, *13*, 839–846.
10. Mitzi, D. B.; Yuan, M.; Liu, W.; Kellock, A. J.; Chey, S. J.; Deline, V.; Schrott, A. G. A High-Efficiency Solution-Deposited Thin-Film Photovoltaic Device. *Adv. Mater.* **2008**, *20*, 3657–3662.
11. Todorov, T. K.; Reuter, K. B.; Mitzi, D. B. High-Efficiency Solar Cell with Earth-Abundant Liquid-Processed Absorber. *Adv. Mater.* **2010**, *22*, E156–E159.
12. Ford, G. M.; Guo, Q. J.; Agrawal, R.; Hillhouse, H. W. Earth Abundant Element $Cu_2Zn(Sn_{1-x}Ge_x)S_4$ Nanocrystals for Tunable Band Gap Solar Cells: 6.8% Efficient Device Fabrication. *Chem. Mater.* **2011**, *23*, 2626–2629.
13. Kathalingam, A.; Kim, M. R.; Chae, Y. S.; Rhee, J. K.; Thanikaikarasan, S.; Mahalingam, T. Study on Electrodeposited $CdSe_xTe_{1-x}$ Semiconducting Thin Films. *J. Alloys Compd.* **2010**, *505*, 758–761.
14. Islam, R.; Banerjee, H. D.; Rao, D. R. Structural and Optical-Properties of $CdSe_xTe_{1-x}$ Thin-Films Grown by Electron-Beam Evaporation. *Thin Solid Films* **1995**, *266*, 215–218.
15. Bailey, R. E.; Nie, S. M. Alloyed Semiconductor Quantum Dots: Tuning the Optical Properties without Changing the Particle Size. *J. Am. Chem. Soc.* **2003**, *125*, 7100–7106.
16. Muthukumarasamy, N.; Velumani, S.; Balasundaraprabhu, R.; Jayakumar, S.; Kannan, M. D. Fabrication and Characterization of n-$CdSe_{0.7}Te_{0.3}$/p-$CdSe_{0.15}Te_{0.85}$ Solar Cell. *Vacuum* **2010**, *84*, 1216–1219.
17. Murali, K. R. Characteristics of Slurry Coated CdSeTe Films. *Mater. Sci. Semicond. Process.* **2010**, *13*, 193–198.
18. Gabor, A. M.; Tuttle, J. R.; Albin, D. S.; Contreras, M. A.; Noufi, R.; Hermann, A. M. High-Efficiency $CuInGa_{1-x}Se_2$ Solar-Cells made from (In_xGa_{1-x})$_2Se_3$ Precursor Films. *Appl. Phys. Lett.* **1994**, *65*, 198–200.
19. Contreras, M. A.; Tuttle, J.; Gabor, A.; Tennant, A.; Ramanathan, K.; Asher, S.; Franz, A.; Keane, J.; Wang, L.; Noufi, R. High Efficiency Graded Bandgap Thin-Film Polycrystalline Cu(In,Ga)Se_2-Based Solar Cells. *Sol. Energy Mater. Sol. Cells* **1996**, *41−2*, 231–246.
20. Dullweber, T.; Hanna, G.; Rau, U.; Schock, H. W. A New Approach to High-Efficiency Solar Cells by Band Gap Grading in Cu(In,Ga)Se_2 Chalcopyrite Semiconductors. *Sol. Energy Mater. Sol. Cells* **2001**, *67*, 145–150.
21. Schlenker, C. W.; Barlier, V. S.; Chin, S. W.; Whited, M. T.; McAnally, R. E.; Forrest, S. R.; Thompson, M. E. Cascade Organic Solar Cells. *Chem. Mater.* **2011**, *23*, 4132–4140.
22. Kramer, I. J.; Levina, L.; Debnath, R.; Zhitomirsky, D.; Sargent, E. H. Solar Cells Using Quantum Funnels. *Nano Lett.* **2011**, *11*, 3701–3706.
23. Xie, R.; Rutherford, M.; Peng, X. Formation of High-Quality I−III−VI Semiconductor Nanocrystals by Tuning Relative Reactivity of Cationic Precursors. *J. Am. Chem. Soc.* **2009**, *131*, 5691–5697.
24. McGill, T., Sotomayor Torres, C., Gebhardt, W., Eds. *Growth and Optical Properties of Wide-Gap II−VI Low-Dimensional Semiconductors*; Plenum Press: New York, 1989; p 67.
25. Muthukumarasamy, N.; Balasundaraprabhu, R.; Jayakumar, S.; Kannan, M. D. Investigations on Structural Phase Transition in Hot Wall Deposited $CdSe_xTe_{1-x}$ Thin Films. *Mater. Chem. Phys.* **2007**, *102*, 86–91.
26. More, P. D.; Shahane, G. S.; Deshmukh, L. P.; Bhosale, P. N. Spectro-structural Characterisation of $CdSe_{1-x}Te_x$ Alloyed Thin Films. *Mater. Chem. Phys.* **2003**, *80*, 48–54.
27. Zhao, X.; Wanga, X.; Lin, H.; Wang, Z. Relationships between Lattice Energy and Electronic Polarizability of ANB8-N Crystals. *Opt. Commun.* **2010**, *283*, 1668–1673.
28. Adachi, S. *Properties of Group-IV, III−V and II−VI Semiconductors*; John Wiley and Sons Ltd., New York, 2005.

29. Bailey, J. E.; Hirsch, P. B. The Recrystallization Process in Some Polycrystalline Metals. *Proc. R. Soc. London, Ser. A* **1962**, *267*, 11–30.
30. Chi, C.-F.; Liau, S.-Y.; Lee, Y.-L. The Heat Annealing Effect on the Performance of CdS/CdSe-Sensitized TiO_2 Photoelectrodes in Photochemical Hydrogen Generation. *Nanotechnology* **2010**, *21*, 025202.
31. Wang, F.; Schwartzman, A.; Fahrenbruch, A. L.; Sinclair, R.; Bube, R. H.; Stahle, C. M. Kinetics and Oxide Composition for Thermal-Oxidation of Cadmium Telluride. *J. Appl. Phys.* **1987**, *62*, 1469–1476.
32. McCandless, B. E.; Sites, J. R. Cadmium Telluride Solar Cells. In *Handbook of Photovoltaic Science and Engineering*, 2nd ed.; Luque, A., S., H., Ed.; John Wiley & Sons: New York, 2011.
33. Van Vechten, J.; Bergstresser, T. Electronic Structures of Semiconductor Alloys. *Phys. Rev. B* **1970**, *1*, 3351–3358.
34. Feng, Z. C.; Becla, P.; Kim, L. S.; Perkowitz, S.; Feng, Y. P.; Poon, H. C.; Williams, K. P.; Pitt, G. D. Raman, Infrared, Photoluminescence and Theoretical-Studies of the II−VI−I Ternary CdSeTe. *J. Cryst. Growth* **1994**, *138*, 239–243.
35. Hannachi, L.; Bouarissa, N. Electronic Structure and Optical Properties of $CdSe_{(x)}Te_{(1-x)}$ Mixed Crystals. *Superlat. Microstruct.* **2008**, *44*, 794–801.
36. Benamar, E.; Rami, M.; Fahoume, M.; Chraibi, F.; Ennaoui, A. Electrodeposition and Characterization of $CdSe_xTe_{1-x}$ Semiconducting Thin Films. *Solid State Sci.* **1999**, *1*, 301–310.
37. Wu, J.; Walukiewicz, W.; Yu, K. M.; Ager, J. W.; Li, S. X.; Haller, E. E.; Lu, H.; Schaff, W. J. Universal Bandgap Bowing in Group-III Nitride Alloys. *Solid State Commun.* **2003**, *127*, 411–414.
38. Tit, N.; Obaidat, I. M.; Alawadhi, H. Origins of Bandgap Bowing in Compound-Semiconductor Common-Cation Ternary Alloys. *J. Phys.: Condens. Matter* **2009**, *21*.
39. Jasieniak, J.; Califano, M.; Watkins, S. E. Size-Dependent Valence and Conduction Band-Edge Energies of Semiconductor Nanocrystals. *ACS Nano* **2011**, *5*, 5888–5902.
40. McCandless, B. E.; Hegedus, S. S.; Birkmire, R. W.; Cunningham, D. Correlation of Surface Phases with Electrical Behavior in Thin-Film CdTe Devices. *Thin Solid Films* **2003**, *431*, 249–256.
41. Yu, W. W.; Peng, X. G. Formation of High-Quality CdS and Other II−VI Semiconductor Nanocrystals in Noncoordinating Solvents: Tunable Reactivity of Monomers. *Angew. Chem., Int. Ed.* **2002**, *41*, 2368–2371.
42. van Embden, J.; Mulvaney, P. Nucleation and Growth of CdSe Nanocrystals in a Binary Ligand System. *Langmuir* **2005**, *21*, 10226–10233.
43. Wood, A.; Giersig, M.; Hilgendorff, M.; Vilas-Campos, A.; Liz-Marzan, L. M.; Mulvaney, P. Size Effects in ZnO: The Cluster to Quantum Dot Transition. *Aust. J. Chem.* **2003**, *56*, 1051–1057.
44. Horcas, I.; Fernandez, R.; Gomez-Rodriguez, J. M.; Colchero, J.; Gomez-Herrero, J.; Baro, A. M. WSXM: A Software for Scanning Probe Microscopy and a Tool for Nanotechnology. *Rev. Sci. Instrum.* **2007**, *78*, 013705.
45. Giannuzzi, L. A.; Drown, J. L.; Brown, S. R.; Irwin, R. B.; Stevie, F. Applications of the FIB Lift-Out Technique for TEM Specimen Preparation. *Microsc. Res. Tech.* **1998**, *41*, 285–290.